Edelweiss Applied Science and Technology
ISSN: 2576-8484
Vol. 8, No. 6, 3902-3924
2024
Publisher: Learning Gate
DOI: 10.55214/25768484.v8i6.2846

Comparative numerical study of the energy performance of two different configurations of a hybrid photovoltaic/thermal air collector

Yao Kombate[1,2*], Kokou N'wuitcha[1,2], Komlan Déla Donald Aoukou[2], Koffi Gagnon Apedanou[2], Yendouban Kolani[2], N'Gissa Attah[2], Bernard Obese[3]
[1]Regional Center of Excellence for Electricity Management (CERME), University of Lomé (UL), Lomé, Togo; yao.kombate@cerme-togo.org (Y.K.) knwuitcha@gmail.com (K.N.W.)
[2]Solar Energy Laboratory, Department of Physics, Faculty of Sciences, University of Lomé (UL), Lomé, Togo; aaoukou@yahoo.fr (K.D.D.A.) gagnonjoseph@yahoo.fr (K.G.A.) yendoubankolani@gmail.com (Y.K.) attahalexis13@gmail.com (N.G.A.)
[3]Department of Science Education, University of Cape Coast, Cape Coast, Ghana; bernard.obese@stu.ucc.edu.gh (B.O.)

Abstract: Solar energy is a renewable alternative to fossil fuels. When solar energy is converted into electricity by photovoltaic (PV) solar modules, the heat generated increases the temperature of the PV solar cells and, as a result, reduces their electrical efficiency. Several techniques are used to cool PV solar cells in order to reduce their operating temperature. One technique is the use of hybrid photovoltaic/thermal (PVT) solar collectors, which simultaneously produce electricity and useful heat. In the airflow channel, the heat and mass transfer equations and those derived from the energy balance on the solid layers of the collector were discretized using the finite difference method with an implicit alternating directions (ADI) scheme. All the algebraic equations obtained after discretization were solved using the Thomas algorithm. The aim is to make a numerical comparison of the energy performance of the Verre-PV-Tedlar and Verre-PV-Verre flat-plate air PVT hybrid solar collectors in the climatic conditions of Lomé, Togo. Under the same operating conditions, the average electrical efficiencies of the Verre-PV-Verre and Verre-PV-Tedlar flat-plate air PVT hybrid collectors are 15.34% and 13.85% respectively. There is a 1.49% improvement in electrical efficiency for a Verre-PV-Verre air-source PVT hybrid collector compared with a Verre-PV-Tedlar PVT hybrid collector. The Verre-PV-Verre flat plate PVT air hybrid collector has an average daily electrical energy gain of 0.564 kWh and a thermal energy gain of 0.839 kWh, while the Verre-PV-Tedlar flat plate PVT air hybrid collector has an average daily electrical energy gain of 0.548 kWh and a thermal energy gain of 1.403 kWh.
Keywords: *Cooling, Electrical energy, Glass-PV-Glass, Glass-PV-Tedlar, Modelling, energy performance, PVT hybrid solar collector.*

1. Introduction

Climate change, energy security, economic growth and the depletion of fossil fuels are driving many countries to turn to solar energy as a reliable and secure alternative energy source. Solar energy is currently one of the fastest growing renewable energy sources in the world [1]. The electrical energy generated by photovoltaic (PV) solar cells and the thermal energy produced by solar thermal collectors are the two main ways of using solar energy. The idea behind the design of hybrid photovoltaic/thermal (PVT) solar collectors is to reduce the operating temperature of PV solar cells in order to improve their electrical performance. The PVT hybrid air collector is one of the most widely used PV module cooling technologies in recent years. The forced circulation of channeled air cools the PV solar cells and recovers unwanted heat from them as useful heat [2]. This system can be used for domestic, agricultural and industrial applications [3]. As a result, PVT hybrid solar collectors can achieve a higher overall efficiency than using PV solar modules and thermal solar collectors alone [4, 5]. Several studies on the design of PVT hybrid solar collectors with different configurations have been carried out

* Correspondence: yao.kombate@cerme-togo.org

in recent years. Moreover, improvements in the electrical and thermal performance of these different PVT hybrid solar collector configurations are difficult to achieve simultaneously [6], [7]. It is therefore advisable to take two factors into account when choosing the best PVT hybrid collector configuration: the user's priority energy need and the cost-benefit of each PVT hybrid collector configuration [7]. Dadioti [8] has studied the parameters that influence the optimum performance of PVT hybrid solar collectors. The results obtained showed that glazed air PVT hybrid solar collectors with a single cover proved to be the optimal configuration for residential applications where electricity production is a priority [8].

In order to reduce heat loss from the top surface of the PVT planar air hybrid solar collector, PVT air hybrid solar collectors with single or double glazing and insulating materials are used. Glass covers and insulation are placed on the front or back of the PV solar cells to reduce convection and radiation losses to the atmosphere [6]. This reduction in heat loss will optimize the energy performance of PVT hybrid solar collectors. A study by Ranganathan et al. [9] showed that the maximum temperature of the top glass, PV solar cells, Tedlar and air at the air duct outlet are 56.06°C, 59.44°C and 45.48°C respectively [9]. An experimental study by Tiwari and Sodha [10] evaluated the overall performance of different configurations of unglazed and glazed PVT hybrid air collectors, with and without Tedlar. The results showed that the hybrid PVT air-glazed solar collector without Tedlar gives a better overall performance [10]. Joshi et al. [11] compared the performance of an unglazed PVT hybrid air collector with a glass-Tedlar and glass-glass PVT hybrid air collector. The back surface temperature was higher in the glass-glass PVT hybrid collector than in the glass-Tedlar PVT hybrid collector. The results showed that the glass-glass PVT hybrid collector has the best thermal efficiency, around 15.7% to 18.3% compared with 13.4% to 16.5% for the glass-Tedlar PVT hybrid collector, and a better overall efficiency of 43.4% to 47.4% compared with 41.6% to 45.4% for the glass-Tedlar PVT hybrid collector [11]. Kim and Kim [12] have shown that the thermal efficiency of the glazed air PVT hybrid solar collector is 14%, higher than that of the unglazed air PVT hybrid solar collector, while the unglazed air PVT hybrid solar collector has an electrical efficiency of 1.4% higher than that of the glazed air PVT hybrid solar collector. According to Slimani [13], the use of glazing in a double-pass PVT hybrid solar collector offers very high energy efficiency. The thermal and electrical efficiencies obtained under indoor conditions are 76% and 9.9% respectively [13]. Similarly, Hussain and Kim [14] evaluated the energy performance of two configurations of the semi-transparent dual-fluid PVT hybrid collector, the configuration with glass-to-glass protection under the PV solar cells and the configuration with glass-to-PV cell backsheet protection. The results showed that the PVT hybrid collector with a glass-to-glass configuration extracts additional heat from the PV solar cells and thus improves its overall energy transfer efficiency. The electrical and thermal efficiencies with the glass-glass configuration are 14.31% and 52.22% respectively and with the glass-backsheet-PV cell configuration, the latter are 13.92% and 48.25% respectively [14].

Hegazy et al. [15] studied three different configurations of a PVT hybrid solar collector with double-pass fins. In the first configuration, the PV solar module was placed on the absorber plate of the solar thermal collector. In the second configuration, the PV module was placed next to the glass cover of the solar thermal collector, while in the third, the PV module was completely separated from the solar thermal collector. The third system configuration had the highest overall performance. The daily thermal efficiencies of the first, second and third hybrid system configurations were 53%, 27% and 64% respectively at a mass flow rate of 0.02 kg/s [15]. Beniwal [16] showed that the electrical efficiency of the semi-transparent air PVT hybrid solar collector is higher than that of the opaque air PVT hybrid solar collector and the electrical efficiency of the opaque air PVT hybrid solar collector decreases. This decrease is due to the higher operating temperature of the PV module because of the thermal conduction of the Tedlar [16]. According to El-Hamid et al. [17], modifying the structure of the planar PVT hybrid air collector by removing the top glass layer or by adding an air gap with a top glass layer or by creating a double-pass channel for cooling the PV solar cells, effectively improves the overall performance of the PVT hybrid collector. In fact, these authors carried out a comparative study of the influence of the layout of the absorber plate, the addition of top and bottom protective glass and the configuration of the airflow channel. The average daily energy and exergy efficiencies obtained were

85.06% and 13.92% respectively for the single-glazed, double-pass PVT hybrid collector and 82.12% and 12.95% for the double-glazed, double-pass PVT hybrid collector. In addition, the single-pass double-glazed configuration with the air gap had the lowest thermal and electrical efficiencies [17]. Hossain et al. [18] designed a new type of heat exchanger for PVT hybrid solar systems and experimentally studied the performance of the system in comparison with an identical PV solar panel under outdoor conditions in Dhaka, Bangladesh. The experiments showed that the highest improvement in open circuit voltage was 1.3V. In addition, the overall improvement in power output of the solar PV panel was 2.5 W [18]. Nahar et al. [19] numerically demonstrated that the fluid flow channel can be directly attached to the back of the PV module using a thermally conductive paste without the presence of the absorber plate. Numerical results showed that the temperature of the PV cells decreases by 42°C on average and that the electrical efficiency and electrical power increase by 2% and 20 W, respectively, for the aluminum and copper channels when the fluid inlet velocity is increased from 0.0009 m/s to 0.05 m/s. The use of copper or aluminum as the material for the fluid flow channel results in better and similar performance as the PVT hybrid collector [20]. It has also been shown that a confined air space under the glass cover and above the PV module creates a greenhouse effect. In fact, when there is little sunlight, the confined layer of air has a significant effect on thermal efficiency. For example, for solar radiation of 300 W/m², the greenhouse effect increases thermal efficiency by 12% compared with the case where it is ignored, but has no significant effect on electrical efficiency [21].

Insulation is of paramount importance when designing a PVT hybrid solar collector. Thermal insulation materials, placed on the back surface and edges of the absorber, significantly reduce heat loss from the back and edges of the collector [22]. Although the insulation materials can significantly reduce heat loss to the outside, there can still be significant heat loss. Heat loss through the bottom insulation layer is mainly due to thermal conduction and convection. Some unglazed PVT air hybrid solar collectors have no back insulation and others have back insulation. The optimum thickness of insulation on the back of the absorber is between 0.05 m and 0.15 m and the impact of the emittance of infrared radiation on the efficiency of a collector is more noticeable when there is a single glass cover than a hybrid solar collector without a cover [23].

Based on the above literature review, it has been shown that the modification of the airflow direction and the addition of the glazing influences the electrical and thermal performance of the planar PVT hybrid air collector technology. To the best of our knowledge, no study has been reported on the glazed flat plate PVT hybrid air collector with glass-to-glass protection in front of and behind the PV solar cells instead of Tedlar in the case of two-dimensional dynamic laminar flow. In this paper, a comparative numerical analysis of the effect of the presence of Tedlar (back layer of PV solar cells) and its replacement by a lower protective glass layer has been studied. The main objective is to determine the temperature distribution of the PV solar cells and the fluid in order to numerically analyze the energy performance of the glass-PV-Tedlar and glass-PV-glass air-source PVT hybrid solar collector under the climatic conditions of Lomé, Togo.

2. Materials and Numerical Method

2.1. Physical Model and Thermophysical Properties

The physical model of our study system is an air-cooled PVT hybrid solar collector consisting of a PV solar module and a heat exchanger in two different configurations, as shown in Figure 1.

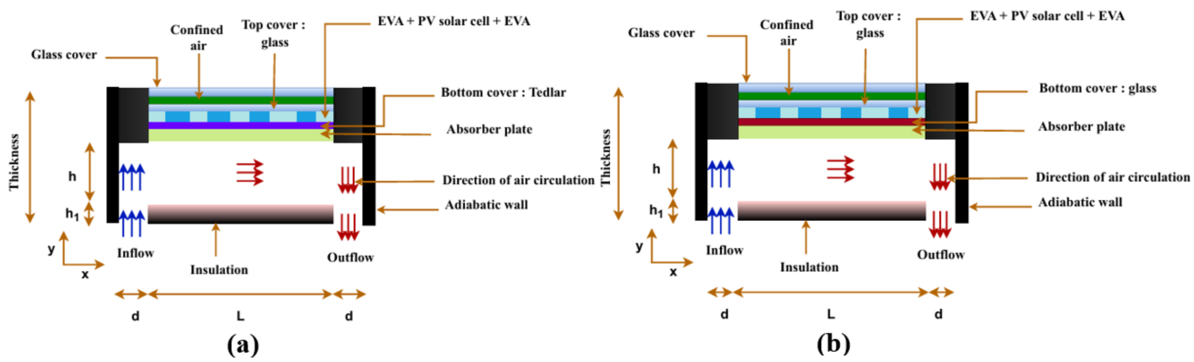

Figure 1.
Front view of the PVT hybrid air collector: (a) Glass-PV-Tedlar and (b) Glass-PV-Glass.

The flat-plate PVT hybrid air collector consists of the glass cover, the confined air layer, the glass top cover, the PV layer (two layers of ethylene vinyl acetate (EVA) and monocrystalline solar cell), the Tedlar or glass bottom cover, the rectangular heat exchanger and the insulation (glass wool). The absorber plate is attached directly to the back of the monocrystalline PV solar module using thermally conductive adhesive. The geometric and physical properties of the LX-100M PV module are used in this numerical investigation. The PV module has 36 monocrystalline solar cells, each with a size of 125×125 mm, maximum power output of 100 W, weight of 7.8 kg, dimensions (1194×542×35 mm), voltage at maximum power point 18.70 V, current at maximum power point 5.39 A, open-circuit voltage 21.60 V and short-circuit current 5.87 A. The thermophysical and optical properties of the system are listed in Tables 1 and 2.

Table 1.
Thermophysical properties of the PVT hybrid solar collector [10, 24-26].

PVT hybrid collector layers	PVT hybrid collector dimensions (m)	Thermal conductivity (W/m. K)	Density (kg/m^3)	Specific heat (J/kg. K)
Glass	1.2×0.542×0.003	1.1	2700	840
Confined air	1.2×0.542×0.02	0.026	1.184	1007
PV solar cells	1.2×0.542×0.0003	0.036	2330	700
Tedlar	1.2×0.542×0.0005	0.2	1200	1250
Thermal paste	1.2×0.542×0.0003	1.9	2600	700
Air (Fluid region)	1.2×0.542×0.3	0.026	1.184	1007
Absorber (Steel sheet)	1.2×0.542×0.002	54	7833	465
Insulation	1.2×0.542×0.05	0.041	15	880

Table 2.
Optical properties of the PVT hybrid solar collector [10, 15, 24].

Optical properties	Value
Absorptivity of glass (α_g)	0.05
Glass emissivity (ε_g)	0.88
Transmissivity of glass (τ_g)	0.90
Absorptivity of PV cells (α_{pv})	0.95
Absorptivity of Tedlar (α_{td})	0.80
Absorber emissivity (ε_p)	0.95
Emissivity of insulation (ε_{ins})	0.90

2.2. Simplifying Assumptions

In order to simplify our mathematical model, the main assumptions used in the mathematical model are as follows:

- The fluid is laminar and its flow in the channel is incompressible in the dynamic regime;
- The fluid flow is two-dimensional;
- Heat transfer in the different layers of the PVT hybrid collector is two-dimensional;
- All side walls of the PVT hybrid solar collector are considered to be adiabatic;
- The thermophysical properties of the fluid depend on the fluid temperature;
- The thermophysical properties of the solid layers remain constant throughout the operation of the PVT hybrid collector.

1.3. Mathematical Model of the Two Different Configurations

The mathematical models combine the thermal model of the air circulating in the duct and the thermal model in the different layers of the two configurations of the planar PVT hybrid air collector. In the solid domains, heat transfer occurs by conduction, whereas in the fluid, heat transfer is conjugate, i.e. dominated by convection with a contribution from conduction. The different heat transfers between the layers and between the solid layers and the fluid are summarized in Figure 2.

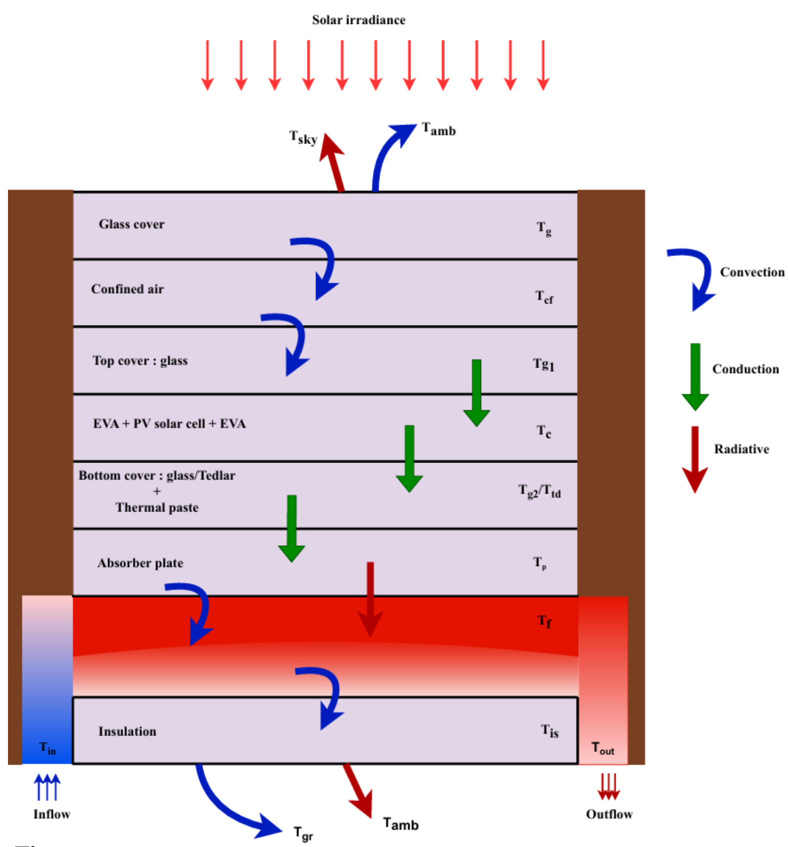

Figure 2.
Different heat transfer mechanisms in the PVT air-source hybrid solar collector.

2.2.1. Basic Equations in the Fluid Zone and Boundary Conditions

Based on the assumptions made, the transfer equations and boundary conditions are written with the following dimensionless variables:

ISSN: 2576-8484
Vol. 8, No. 6: 3902-3924, 2024
DOI: 10.55214/25768484.v8i6.2846

$$\begin{cases} X = \frac{x}{L},\ Y = \frac{y}{L},\ U_f = \frac{u_f}{V_0},\ V_f = \frac{v_f}{V_0} \\ \theta = \frac{T_f - T_{min}}{\Delta T_{ref}} = \frac{T_f - T_{min}}{T_{pv} - T_{min}},\ \tau = \frac{V_0 t}{L} \\ C_f = \frac{c_f - c_{min}}{\Delta c_{ref}} = \frac{c_f - c_{min}}{c_{max} - c_{min}},\ \Omega_f = \frac{\omega_f L}{V_0},\ \Psi_f = \frac{\psi_f}{V_0 L} \end{cases} \tag{1}$$

- Vorticity, current function and velocity fields equations

$$\frac{\partial \Omega_f}{\partial \tau} + U_f \frac{\partial \Omega_f}{\partial X} + V_f \frac{\partial \Omega_f}{\partial Y} = \frac{1}{R_e}\left(\frac{\partial^2 \Omega_f}{\partial X^2} + \frac{\partial^2 \Omega_f}{\partial Y^2}\right) + R_{iT}\left[\cos\gamma \frac{\partial \theta_f}{\partial X} - \sin\gamma \frac{\partial \theta_f}{\partial Y}\right] + R_{ic}\left[\cos\gamma \frac{\partial C_f}{\partial X} - \sin\gamma \frac{\partial C_f}{\partial Y}\right] \tag{2}$$

$$\Omega_f = -\left(\frac{\partial^2 \Psi_f}{\partial X^2} + \frac{\partial^2 \Psi_f}{\partial Y^2}\right) \tag{3}$$

$$\Omega = \frac{\partial V_f}{\partial X} - \frac{\partial U_f}{\partial Y}\ ;\ U_f = \frac{\partial \Psi_f}{\partial Y}\ ;\ V_f = -\frac{\partial \Psi_f}{\partial X} \tag{4}$$

- Energy equation in the fluid

$$\frac{\partial \theta_f}{\partial \tau} + U_f \frac{\partial \theta_f}{\partial X} + V_f \frac{\partial \theta_f}{\partial Y} = \frac{1}{R_e \times P_r}\left(\frac{\partial^2 \theta_f}{\partial X^2} + \frac{\partial^2 \theta_f}{\partial Y^2}\right) \tag{5}$$

- Humidity diffusion equation

$$\frac{\partial C_f}{\partial \tau} + U_f \frac{\partial C_f}{\partial X} + V_f \frac{\partial C_f}{\partial Y} = \frac{1}{S_c \times R_e}\left(\frac{\partial^2 C_f}{\partial X^2} + \frac{\partial^2 C_f}{\partial Y^2}\right) \tag{6}$$

with:

x, y : cartesian coordinate axes (m) ; X, Y : dimensionless coordinate axes ; u, v : components of the fluid velocity vectors in the x and y directions (m.s^{-1}) ; U_f, U_f : dimensionless velocities in the x and y directions respectively ; c_f : mass fraction of the air vapor or moisture (kg water/kg dry air) ; c_{fe} : fluid moisture near the plate (kg water/kg dry air) ; c_a : concentration in the fluid away from the plate (kg water/kg dry air); C_f : moisture or dimensionless concentration ; T_f : temperature of the plate (°C) ; T_{fe} : temperature of the fluid near the plate (°C) ; T_a : temperature of the fluid far from the plate (°C) ; θ_f : temperature of the fluid dimensionless ; t : time (s) ; τ : time dimensionless ; γ : angle of inclination of the hybrid solar collector PVT with respect to horizontal (°C); $R_e = \frac{\rho L V_0}{\mu}$: the number of Reynolds; $P_r = \frac{\mu C_p}{\lambda}$: the number of Prandtl ; $R_{i_T} = \frac{g\beta_T L \Delta T}{{V_0}^2}$: the Richardson number related to temperature; $R_{i_C} = \frac{g\beta_c L \Delta c}{{V_0}^2}$: the Richardson number related to humidity; $Sc = \frac{\nu}{D}$: the Schmidt number.

The conditions for dimensionless limits are as follows:

(1) Initial condition: $\tau = \tau_0$

$$U_f = V_f = 0, \Omega_f = 0, \Psi_f = 0, \theta_f = 0, C_f = 0 \tag{7}$$

(2) Boundary conditions at the inlet of the air flow channel: $0 < X < \frac{d}{L}$ et $Y = 0$

$$U_f = 0\ ; V_f = 1\ ; \Psi_f = -X\ ; \theta_f = 0\ ; C_f = 0\ ;\ \Omega_f = -\left.\frac{\partial^2 \Psi_f}{\partial Y^2}\right|_{X,Y=0} \tag{8}$$

(3) Boundary conditions at the outlet of the air flow channel: $1 - \frac{d}{L} < X < 1\ ;\ Y = 0$

$$\left.\frac{\partial U_f}{\partial Y}\right|_{X,Y=0} = \left.\frac{\partial V_f}{\partial Y}\right|_{X,Y=0} = 0\ ;\ \left.\frac{\partial \theta_f}{\partial Y}\right|_{X,Y=0} = 0\ ;\ \left.\frac{\partial C_f}{\partial Y}\right|_{X,Y=0} = 0\ ;\left.\frac{\partial \Psi_f}{\partial Y}\right|_{X,Y=0} = 0;$$

$$\left.\frac{\partial \Omega_f}{\partial Y}\right|_{X,Y=0} = 0 \tag{9}$$

(4) Boundary conditions at the inside walls of the air duct:

- Adiabatic wall at the air duct inlet: $X = 0\ ;\ 0 < Y < \frac{H}{L}$

$$U_f = V_f = 0\ ;\ \left.\frac{\partial \theta_f}{\partial X}\right|_{X=0,Y} = 0\ ;\ \left.\frac{\partial C_f}{\partial X}\right|_{X=0,Y} = 0; \Psi_f = 0\ ; \Omega_f = -\left.\frac{\partial^2 \Psi_f}{\partial X^2}\right|_{X=0,Y} \tag{10}$$

- Insulation wall at the entrance of the duct: $X = \frac{d}{L}\ ;\ 0 < Y < \frac{H_1}{L}$

$$U_f = V_f = 0\ ;\ \left.\frac{\partial \theta_f}{\partial X}\right|_{X=\frac{d}{L},Y} = 0\ ;\ \left.\frac{\partial C_f}{\partial X}\right|_{X=\frac{d}{L},Y} = 0;\ \Psi_f = -\frac{d}{L}\ ; \Omega_f = -\left.\frac{\partial^2 \Psi_f}{\partial X^2}\right|_{X=\frac{d}{L},Y} \tag{11}$$

- Insulation part at the outlet of the conduit: $X = 1 - \frac{d}{L}\ ;\ 0 < Y < \frac{H_1}{L}$

$$U_f = V_f = 0\ ;\ \left.\frac{\partial \theta_f}{\partial X}\right|_{X=1-\frac{d}{L},Y} = 0\ ;\ \left.\frac{\partial C_f}{\partial X}\right|_{X=1-\frac{d}{L},Y} = 0\ ;\ \Psi_f = -\frac{d}{L}\ ;\ \Omega_f = -\left.\frac{\partial^2 \Psi_f}{\partial X^2}\right|_{X=1-\frac{d}{L},Y} \tag{12}$$

- Adiabatic wall at the outlet of the duct: $X = 1\ ; 0 < Y < \frac{H}{L}$

$$U_f = V_f = 0\ ; \left.\frac{\partial \theta_f}{\partial X}\right|_{X=1,Y} = 0\ ; \left.\frac{\partial C_f}{\partial X}\right|_{X=1,Y} = 0;\ \Psi_f = 0\ ;\ \Omega_f = -\left.\frac{\partial^2 \Psi_f}{\partial X^2}\right|_{X=1,Y} \tag{13}$$

- Bottom-air heat exchanger wall interface: $\frac{d}{L} < X < 1 - \frac{d}{L}\ ;\ Y = \frac{H_1}{L}$

$$U_f = V_f = 0\ ;\ \theta_f = \theta_{ins}\ ; \left.\frac{\partial C_f}{\partial Y}\right|_{X,Y=\frac{H_1}{L}} = 0; \Psi_f = -\frac{d}{L};\ \Omega_f = -\left.\frac{\partial^2 \Psi_f}{\partial Y^2}\right|_{X,Y=\frac{H_1}{L}} \tag{14}$$

- Upper-air heat exchanger interface wall: $0 < X < 1\ ;\ Y = \frac{H}{L}$

$$U_f = V_f = 0;\ \Psi_f = 0;\ \Omega_f = -\left.\frac{\partial^2 \Psi_f}{\partial Y^2}\right|_{X,Y=\frac{H}{L}} ; \theta_f = \theta_p\ ; \left.\frac{\partial C_f}{\partial Y}\right|_{X,Y=\frac{H}{L}} = 0 \tag{15}$$

2.2.2. Basic Equations in Solid Layers

The solid-layer mathematical model of the hybrid PVT air plane collector is obtained by applying the energy conservation principle of the system. The energy equations take into account the rate of change in the system's internal energy, the rate of energy input, the rate of energy output and the rate of energy generated within the different layers of the PVT collector [19, 27].

$$\frac{dE(x,y,t)}{dt} = E_e - E_s + \dot{Q} \tag{16}$$

where $\frac{dE}{dt}$ is the variation of internal energy in the system, E_e is the rate of heat transfer in the system, E_s is the rate of heat transfer out of the system, $\dot{Q}$ is the rate of heat generation in the solar system. The energy equations for the different layers of the solar system are as follows:

(a) Glass cover energy equation

$$\rho_g e_g C_g \frac{\partial T_g}{\partial t} = \alpha_g G - h_{g-ciel}^{ray}\left(T_g - T_{ciel}\right) - h_{g-g_1}^{ray}\left(T_g - T_{g_1}\right) - h_{g-amb}^{conv}\left(T_g - T_{amb}\right)$$
$$-h_{g-cf}^{conv}\left(T_g - T_{cf}\right) + \lambda_g e_g \left(\frac{\partial^2 T_g}{\partial x^2} + \frac{\partial^2 T_g}{\partial y^2}\right) \tag{17}$$

where α_g is the absorption coefficient of the glass cover; G is solar irradiance; h_{g-amb}^{cv} is the convection coefficient between the glass cover and ambient air; h_{g-cf}^{cv} is the convection coefficient between the glass cover and confined air; $h_{g-g_1}^{rd}$ is the radiation coefficient between the glass cover and the top cover; h_{g-sky}^{rd} is the radiative coefficient between the glass cover and the sky; T_g, T_{amb}, T_{g_1}, T_{cf} et T_s are the temperature of the glass cover, the ambient temperature, the temperature of the top cover, the temperature of the confined air and the equivalent temperature of the sky, respectively; λ_g is the thermal conductivity of the glass cover; e_g is the thickness of the glass cover; ρ_g is the density of the glass cover; C_g is the mass heat of the glass cover and $\frac{\partial^2 T_g}{\partial x^2} + \frac{\partial^2 T_g}{\partial y^2}$ is the temperature distribution in the glass cover.

(b) Energy equation of confined air

$$\rho_{cf} e_{cf} C_{cf} \frac{\partial T_{cf}}{\partial t} = -h_{cf-g}^{cv}\left(T_{cf} - T_g\right) - h_{cf-g_1}^{cv}\left(T_{cf} - T_{g_1}\right) + \lambda_{cf} e_{cf}\left(\frac{\partial^{2T}{}_{cf}}{\partial x^2} + \frac{\partial^2 T_{cf}}{\partial y^2}\right) \quad (18)$$

where $h_{g_1-cf}^{cv}$ is the convection coefficient of the upper protective glass and the air contained; T_{g_1} is the temperature of the upper cover λ_{cf} is the thermal conductivity of the air; e_{cf} is the thickness of the air contained; ρ_{cf} is the density of the air; C_{cf} is the mass heat of air and $\frac{\partial^2 T_{cf}}{\partial x^2} + \frac{\partial^2 T_{cf}}{\partial y^2}$ is the temperature distribution in the layer in the confined air.

(b) Upper cover energy equation: glass

$$\rho_{g_1} e_{g_1} C_{g_1} \frac{\partial T_{g_1}}{\partial t} = \alpha_g \tau_g G - h_{g_1-v}^{rd}\left(T_{g_1} - T_g\right) - h_{g_1-cf}^{cv}\left(T_{g_1} - T_{cf}\right)$$
$$-h_{g_1-pv}^{cd}\left(T_{g_1} - T_{pv}\right) + \lambda_{g_1} e_{g_1}\left(\frac{\partial^2 T_{g_1}}{\partial x^2} + \frac{\partial^2 T_{g_1}}{\partial y^2}\right) \quad (19)$$

where α_{g_1} is the absorption coefficient of the top cover; τ_g is the transmissivity of the glass cover; T_{pv} is the temperature of the PV cells; $h_{g_1-pv}^{cd}$ is the conduction coefficient between the glass cover and the top cover; λ_{g_1} is the thermal conductivity of the top cover; e_{g_1} is the thickness of the top cover; ρ_{g_1} is the density of the top cover C_{g_1} is the mass heat of the top cover and $\frac{\partial^2 T_{g_1}}{\partial x^2} + \frac{\partial^2 T_{g_1}}{\partial y^2}$ is the temperature distribution in the top cover.

(d) Energy equation of PV solar cells

In the case where the bottom cover is a glass, the energy balance gives equation (20).

$$\rho_{pv} e_{pv} C_{pv} \frac{\partial T_{pv}}{\partial t} = \alpha_{pv} \tau_v^2 \beta G - h_{pv-g_1}^{cd}\left(T_{pv} - T_{g_1}\right) - h_{pv-g_2}^{cd}\left(T_{pv} - T_{g_2}\right)$$
$$+\lambda_{pv} e_{pv}\left(\frac{\partial^2 T_{pv}}{\partial x^2} + \frac{\partial^2 T_{pv}}{\partial y^2}\right) \quad (20)$$

In the case where the bottom cover is Tedlar, the energy balance gives equation (21).

$$\rho_{pv} e_{pv} C_{pv} \frac{\partial T_{pv}}{\partial t} = \alpha_{pv} \tau_v^2 \beta G - h_{pv-g_1}^{cd}\left(T_{pv} - T_{g_1}\right) - h_{pv-td}^{cd}\left(T_{pv} - T_{td}\right)$$
$$+\lambda_{pv} e_{pv}\left(\frac{\partial^2 T_{pv}}{\partial x^2} + \frac{\partial^2 T_{pv}}{\partial y^2}\right) - P_{el,pv} \quad (21)$$

where α_{pv} is the absorptivity of the PV cells; T_{g_2} is the temperature of the lower glass cover; T_{td} is the temperature of the Tedlar; $h_{pv-g_2}^{cd}$ is the coefficient of conduction between the PV cells and the lower glass cover; $h_{\mathrm{pv}-td}^{cd}$ is the conduction coefficient between PV cells and Tedlar; λ_{pv} is the thermal conductivity of the PV cells; e_{pv} is the thickness of the PV module; ρ_{pv} is the density of the PV cells; C_{pv} is the mass heat of the PV cells; $\frac{\partial^2 T_{pv}}{\partial x^2} + \frac{\partial^2 T_{pv}}{\partial y^2}$ is the temperature distribution in PV cells; $P_{el,pv} = \tau_v^2 \beta \eta_{ref}\left[1 - \beta_{pv,ref}\left(T_{pv} - T_{pv}^{ref}\right)\right] \times G$ is the electricity production per unit area of PV solar cells where η_{ref} is the electrical efficiency of the PV cells at reference temperature, $\beta_{pv,ref}$ is the temperature coefficient, T_{pv}^{ref} is the reference temperature and G is solar irradiance and β is the form factor.

(e) Lower cover energy equation: Tedlar

$$\rho_{td} e_{td} C_{td} \frac{\partial T_{td}}{\partial t} = \alpha_{td} \tau_v^2 \tau_{pv} (1 - \beta) G + h_{pv-td}^{cd}\left(T_{pv} - T_{td}\right) - h_{td-p}^{cd}\left(T_{td} - T_p\right)$$
$$+\lambda_{td} e_{td}\left(\frac{\partial^2 T_{td}}{\partial x^2} + \frac{\partial^2 T_{td}}{\partial y^2}\right) \quad (22)$$

where h_{td-p}^{cd} is the conduction coefficient between Tedlar and absorbent plate; λ_{td} is the thermal conductivity of Tedlar; e_{td} is the thickness of Tedlar; ρ_{td} is the density of Tedlar; C_{td} is the mass heat of Tedlar; α_{td} is the absorptivity of Tedlar ; $\frac{\partial^2 T_{td}}{\partial x^2}+\frac{\partial^2 T_{td}}{\partial y^2}$ is the temperature distribution in the Tedlar.

(d) Lower cover energy equation: glass

$$\rho_{g_2} e_{g_2} C_{g_2}\frac{\partial T_{g_2}}{\partial t} = -h_{pv-g_2}^{cd}\left(T_{g_2}-T_{pv}\right)-h_{v_2-p}^{cd}\left(T_{g_2}-T_p\right)+\lambda_{g_2} e_{g_2}\left(\frac{\partial^2 T_{g_2}}{\partial x^2}+\frac{\partial^2 T_{g_2}}{\partial y^2}\right) \tag{23}$$

where $h_{v_2-p}^{cd}$ is the conduction coefficient between the bottom cover and the absorbent plate; λ_{g_2} is the thermal conductivity of the bottom cover; e_{g_2} is the thickness of the bottom cover; ρ_{g_2} is the density mass of the bottom cover; C_{g_2} is the heat mass of the bottom cover and $\frac{\partial^2 T_{g_2}}{\partial x^2}+\frac{\partial^2 T_{g_2}}{\partial y^2}$ is the temperature distribution in the bottom cover.

(e) Energy equation of the absorbent plate

In the case where the bottom cover is Tedlar, the energy balance gives equation (24).

$$\rho_p e_p C_p\frac{\partial T_p}{\partial t} = h_{p-f}^{cv}\left(T_p-T_f\right)-h_{td-p}^{cd}\left(T_p-T_{td}\right)-h_{p-ins}^{rd}\left(T_p-T_{ins}\right)+\lambda_p e_p\left(\frac{\partial^2 T_p}{\partial x^2}+\frac{\partial^2 T_p}{\partial y^2}\right) \tag{24}$$

In the case where the bottom cover is glass, the energy balance gives equation (25).

$$\rho_p e_p C_p\frac{\partial T_p}{\partial t} = h_{p-f}^{cv}\left(T_p-T_f\right)-h_{g_2-p}^{cd}\left(T_p-T_{g_2}\right)-h_{p-ins}^{rd}\left(T_p-T_{ins}\right)+\lambda_p e_p\left(\frac{\partial^2 T_p}{\partial x^2}+\frac{\partial^2 T_p}{\partial y^2}\right) \tag{25}$$

where h_{p-f}^{cv} is the convection coefficient between heat exchanger and fluid; h_{p-ins}^{rd} is the radiation coefficient between absorbent plate and insulator; λ_p is the thermal conductivity of the heat exchanger; e_p is the thickness of the heat exchanger; ρ_p is the density of the heat exchanger; C_p is the mass heat of the heat exchanger and $\frac{\partial^2 T_p}{\partial x^2}+\frac{\partial^2 T_p}{\partial y^2}$ is the temperature distribution in the heat exchanger.

(h) Energy equation for the insulating layer

$$\rho_{ins} e_{ins} C_{ins}\frac{\partial T_{ins}}{\partial t} = -h_{p-ins}^{rd}\left(T_p-T_{ins}\right)-h_{ins-amb}^{cv}\left(T_{ins}-T_{amb}\right)-h_{ins-sol}^{rd}\left(T_{ins}-T_{gr}\right) +\lambda_{ins} e_{ins}\left(\frac{\partial^2 T_{ins}}{\partial x^2}+\frac{\partial^2 T_{ins}}{\partial y^2}\right) \tag{26}$$

where $h_{ins-amb}^{conv}$ is the coefficient of convection between the insulation and the environment; h_{ins-gr}^{rd} is the radiation coefficient between the insulation and the ground; T_{ins} is the temperature of the insulation, λ_{ins} is the conductivity coefficient of the insulation; e_{ins} is the thickness of the insulation; ρ_{ins} is the density of the insulation; C_{ins} is the heat mass of the insulation and $\frac{\partial^2 T_{ins}}{\partial x^2}+\frac{\partial^2 T_{ins}}{\partial y^2}$ is the temperature distribution in the insulation.

2.2.3. Determination of Heat Transfer Coefficients

(a) Coefficient of heat transfer by radiation between the glass cover and the sky [28].

$$h_{g-sky}^{rd} = \varepsilon_g \sigma\left(T_g^2+T_{sky}^2\right)\left(T_g+T_{sky}\right) \tag{27}$$

Where, $\sigma = 5.67.10^{-8} W/m^2.K^4$ and the sky temperature is calculated using Swinbank's formula [29].

$$T_{sky} = 0.0522 \times T_{amb}^{1,5} \tag{28}$$

(b) Coefficient of radiation heat transfer between insulation and soil [27].

$$h_{ins-gr}^{rd} = \frac{\sigma\left(T_{ins}^2+T_{gr}^2\right)\left(T_{ins}+T_{gr}\right)}{\frac{1}{\varepsilon_{ins}}+\frac{1}{\varepsilon_{gr}}-1} \tag{29}$$

(c) Coefficient of radiation heat transfer between the glass cover and the top protective glass [28].

$$h_{g-g_1}^{rd} = \frac{\sigma(T_g^2+T_{g_1}^2)(T_g+T_{g_1})}{\frac{1}{\varepsilon_g}+\frac{1}{\varepsilon_{g_1}}-1} \tag{30}$$

(d) Coefficient of heat transfer by radiation between the absorbing plate and the insolation [28].

$$h_{p-ins}^{rd} = \frac{\sigma(T_p^2+T_{ins}^2)(T_p+T_{ins})}{\frac{1}{\varepsilon_p}+\frac{1}{\varepsilon_{ins}}-1} \tag{31}$$

(e) Convection heat transfer coefficient between the glass cover and the ambient [27, 28].

$$h_{g-amb}^{cv} = 5.7 + 3.8\,V_{wind} \tag{32}$$

(f) Coefficient of heat transfer by convection between the glass cover and the top protective glass [28].

$$h_{cv} = \frac{Nu_{air}\lambda_{air}}{\delta_{air}} \tag{33}$$

Where, Nu_{air}, λ_{air} et δ_{air} represent the Nusselt number, the thermal conductivity of the gap and the distance between the glass cover and the top protective glass. The Nusselt number is calculated using the formula given by Hollands [29].

$$Nu_{air} = 1 + 1.44\left[1 - \frac{1708}{Ra\cos\gamma}\right]^{+} \times \left[1 - \frac{1708(\sin 1.8\gamma)^{1,6}}{Ra\cos\gamma}\right] + \left[\left(\frac{Ra\cos\gamma}{5830}\right)^{\frac{1}{3}} - 1\right]^{+} \tag{34}$$

The Rayleigh number of free convection heat transfer is given by formula (37).

$$R_a = \frac{g\beta_{air}(T_g-T_{g_1})\delta_{gap}^3}{\mu_{air}^2 P_r} \tag{35}$$

Where, g, β_{air}, μ_{air}, P_r, δ_{gap} et $T_g - T_{g_1}$ are the gravity intensity, thermal expansion coefficient, dynamic air viscosity, number of Prandtl, thickness of the confined air layer and temperature difference between the glass cover and the top protective glass respectively.

(g) The heat transfer coefficient of the fluid is defined from the Nusselt of the fluid [28].

$$h_{ins-f}^{cv} = h_{p-f}^{cv} = \frac{Nu_f\lambda_f}{D_h} \tag{36}$$

Where, D_h is the equivalent diameter of the air flow channel.

$$D_h = \frac{4(L\times\ell)}{2\times(L+\ell)} \tag{37}$$

In the case of a laminar flow (Re < 2300), the Nusselt of the fluid is given by [28]:

$$N_{u_f} = 5.4 + \frac{0.00190\left[P_r R_e \frac{D_h}{L}\right]^{1.71}}{1+0.00563\left[P_r R_e \frac{D_h}{L}\right]^{1.17}} \tag{38}$$

(h) The coefficient of heat exchange by conduction between a solid layer i and another solid layer j is given by the following relation [30]:

$$h_{i-j}^{cd} = h_{j-i}^{cd} = \frac{1}{\frac{e_i}{\lambda_i}+\frac{e_j}{\lambda_j}} \tag{39}$$

The thermophysical properties of air vary linearly with temperature according to Ong's assumptions [31].

Specific air heat:

$$C_f = 1.0057 + 0.000066(T_f - 27) \tag{40}$$

Air density:

$$\rho_f = 1.1774 - 0.00359(T_f - 27) \tag{41}$$

Thermal conductivity of air:

$$\lambda_f = 0.02624 + 0.0000758(T_f - 27) \tag{42}$$

Dynamic air viscosity:

$$\mu_f = [1.983 + 0.00184(T_f - 27)] \times 10^{-5} \tag{43}$$

2.4. Evaluation of Energy Performance

(1) The electrical power produced by the sensor is calculated as follows [32]:

$$P_{el,pv} = \eta_{el} A_{PVT} G \tag{44}$$

(2) The electrical efficiency of PV solar cells is related to their operating temperature [32,33].

$$\eta_{el,pv} = \eta_{pv}^{ref} \beta \left[1 - \beta_{pv,ref}\left(T_{pv} - T_{pv}^{ref}\right)\right] \tag{45}$$

(3) The useful thermal power of the PVT hybrid solar collector is calculated by using the product of mass flow, specific thermal capacity of air and difference between outlet and inlet temperature [34].

$$P_{th} = \dot{m} \times C_p \times (T_{out} - T_{in}) \tag{46}$$

(4) The efficiency of the PVT hybrid solar collector is calculated using an equation that gives the relationship between thermal power, solar irradiance and the surface area of the solar collector [34].

$$\eta_{th} = \frac{P_{th}}{G \times A_{PVT}} \tag{47}$$

(5) The total output power of the PVT hybrid solar collector is calculated by adding the electrical output power and the useful thermal output of the PVT hybrid solar collector.

$$P_{tot} = P_{el} + P_{th} \tag{48}$$

(6) The total energy of the PVT hybrid solar collector is calculated by equation (49):

$$E_{tot} = E_{el} + E_{th} \tag{49}$$

(7) The overall efficiency of the PVT hybrid collector is calculated using equation (50).

$$\eta_{PVT} = \eta_{el} + \eta_{th} \tag{50}$$

The electrical kilowatt-hour cannot be directly compared to the thermal kilowatt-hour. In order to account for the quality of energy produced and compare the two forms of energy produced, another approach is to use primary energy efficiency as a more accurate way to evaluate the overall efficiency of the PVT hybrid collector, equivalent thermal efficiency [11, 35]. The aim is to convert conventional electrical efficiency into equivalent thermal efficiency. This indicator takes into account the quantity and quality of solar energy conversion by PVT hybrid solar collectors.

$$\eta_{PVT,EQ} = \frac{\eta_{el}}{C_f} + \eta_{th} \tag{51}$$

where C_f is the average efficiency of electricity generation or conversion factor of the thermal power plant according to the reference country, ranging from 0.20 to 0.40 [35].

3. Numerical Resolution

3.1. Discretization of the Thermal Transfer Equations Within the Fluid

All energy equations are discretized in x and y directions. Indeed, the finite difference method with an implicit alternate-direction (ADI) scheme based on a fractional step pattern with alternating directions, implicit and explicit to discretize the energy equations of the heat transfer fluid. For the solid-layer energy equations of the PVT hybrid collector, the implicit finite difference method was used. All discretized algebraic equations are written in compact form as follows:

$$A_i \phi_{i-1}^{k+1} + B_i \phi_i^{k+1} + C_i \phi_{i+1}^{k+1} = D_i \ \text{with}\ i = 1,\ 2,\ 3,\ \ldots,\ N \tag{52}$$

The discretized energy equations were solved iteratively using the tridiagonal matrix algorithm (TDMA) method called Thomas algorithm. The calculation procedure is written in Fortran 90. The convergence criterion adopted for the numerical solution is when the relative error of the variables Φ (U, V, T, Ω and Ψ) at all points in the study field is less than ε (with $\varepsilon = 10^{-8}$).

$$\left|\frac{\Phi^{n+1} - \Phi^n}{\Phi^{n+1}}\right| \leq \varepsilon \tag{53}$$

Where, n is the number of iterations of the process.

3.2. Choice And Independence of Mesh

Before running the numerical model, it is important to check the independence of the mesh to ensure the accuracy and reliability of the numerical solution. We chose five different mesh sizes, 71×70, 83×78, 95×86, 107×96, 115×103 nodes. The mesh independence test is performed for a Reynolds number of 350 for the two configurations of the PVT planar air hybrid collector studied with a solar radiation intensity of 1000 W/m² and an air inlet temperature of 25°C. The monitoring measurement is carried out on the air temperature at the duct outlet and the temperature of the PV solar cells.

Table 3.
Results of the mesh independence test for the PVT Glass-PV-Tedlar hybrid collector.

Dimensions	**82×73**	**93×79**	**114×86**	**131×92**	**139×99**
Coolant outlet temperature (°C)	44.61	44.03	44.31	44.39	44.90
Solar cell temperature (°C)	63.16	63.27	63.36	63.40	63.44
Computation time (s)	747.554	764.422	844.694	2105.992	2450.140

Table 4.
Results of the mesh independence test for the PVT Glass-PV-Glass hybrid collector.

Dimensions	**82×73**	**93×79**	**114×86**	**131×92**	**139×99**
Coolant outlet temperature (°C)	40.70	40.14	40.25	40.30	40.72
Solar cell temperature (°C)	52.58	52.66	52.72	52.75	52.79
Computation time (s)	371.299	430.246	1184.356	1249.185	2322.859

Tables 3 and 4 show that the PV solar cell temperature and the air outlet temperature in the duct of the PVT Glass-PV-Tedlar hybrid collector and the PVT Glass-PV-Glass hybrid collector are almost the same for all the nodes considered. Therefore, the 82×73 node is used in this study in order to obtain accurate results with a minimum of computation time.

3.3. Model Validation

The present numerical study is validated using the experimental results obtained by Fudholi et al. [36] on a PVT flat plate air hybrid solar collector tested with a solar simulator where the solar irradiance was controlled using a controller. The tests were carried out with five different mass flow rates (0.007 kg/s to 0.07 kg/s) and solar irradiances of 385 W/m² and 820 W/m².

Table 4.
Validation of air outlet temperature with the results of Fudholi et al. [36].

Sunlight irradiance (W/m²)	**Debit (kg/s)**	**Experimental**	**Present data**	**Error (%)** $\left\|\frac{T_{sim}-T_{exp}}{T_{exp}}\right\| \times 100$
385	0.00696	32.2	33.24	3.12
385	0.02492	29.9	31.56	5.12
385	0.03861	29.4	30.94	4.97
385	0.05387	28.4	30.54	7.03
Average				5.06

Table 4 shows the validation of the present model with the experimental results of Fudholi et al. [36] using the air temperature at the channel outlet. A relative deviation of 5.06% between our results and those of Fudholi et al. [36] is obtained for an irradiance of 385 W/m². Our numerical results are therefore in good qualitative agreement with the experimental results of Fudholi et al. [36].

4. Results and Discussion

4.1. Meteorological Data

The meteorological data measured at the Solar Energy Laboratory on 16 March 2024 at the University of Lomé, Togo, are shown in Figure 3. These meteorological data are used in the numerical simulation.

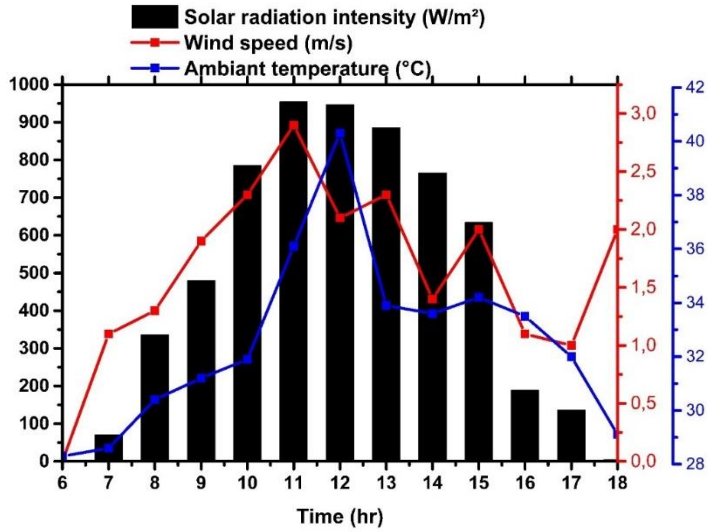

Figure 3.
Variations of ambient conditions for a typical day in March of Lome, Togo.

Incident solar radiation remains perpendicular to the surface of the PV module throughout the day. In fact, the solar radiation measured increased steadily from morning until 11 a.m. to 955 W/m², then gradually decreased until sunset. The ambient temperature measured rose from around 28°C at 6 a.m. to about 40°C at midday, then fell to 29°C at sunset. Wind speed varied throughout the day from 0 m/s to 2.9 m/s. For the numerical simulation, we considered the average wind speed at the surface of the PV module to be 1 m/s.

All the results were obtained with a Reynolds number of 900 (corresponding to a mass flow rate of 0.00967 kg/s), an air inlet temperature of 27°C with solar radiation intensity and ambient temperature varying throughout the day on 16 March 2024.

4.2. Kinematic Study of the Fluid

4.2.1. Analysis of Air Stream Lines

Figure 4 shows the distribution of the flow lines in the heat transfer fluid channel. The distribution of the streamlines reflects the path followed by the fluid as it flows through the heat removal channel in the two configurations of the PVT flat air hybrid collector. Analysis of these flow lines shows that they originate at the inlet and travel towards the outlet, passing near the top of the heat transfer air channel. These open, quasi-parallel streamlines illustrate air flow by forced convection and show by their crowding that this area is the main flow zone.

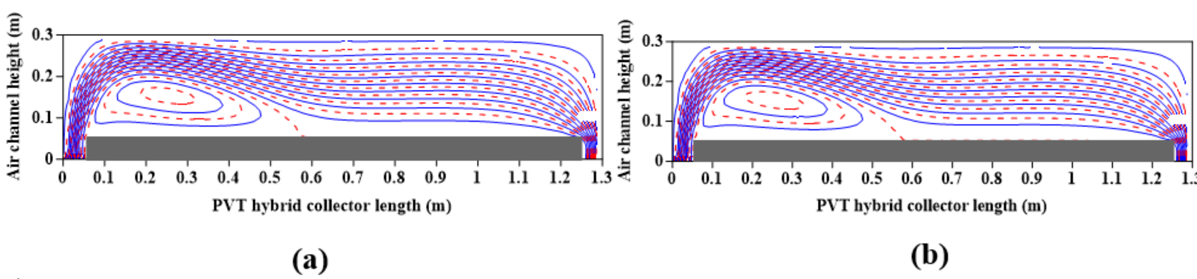

Figure 4.
Distribution of air streamlines: (a) PVT Glass-PVT-Tedlar hybrid air collector; (b) PVT Glass-PVT-Glass hybrid air collector (mass flow rate 0.00967 kg/s, fluid inlet temperature 27°C and wind speed 1 m/s).

Edelweiss Applied Science and Technology
ISSN: 2576-8484
Vol. 8, No. 6: 3902-3924, 2024
DOI: 10.55214/25768484.v8i6.2846

4.2.2. Analysis of Fluid Velocity Profiles

The air velocity profiles at the inlet, inside and outlet of the air flow channel are shown in Figures 5 and 6 for different fluid positions.

Figure 5 shows the curves of the velocity components u and v as a function of the abscissa x for the two configurations. Analysis of Figure 5 (a) shows that the two components have peaks in the vicinity of the inlet and outlet walls and then a plateau in the horizontal part of the heat transfer fluid channel corresponding to very low values. Positive values of u and v near the inlet indicate that the flow is starting to change direction in the channel. Also, the positive u values and the negative v values towards the outlet, reveal a bend in the air flow in the right-hand. These results are corroborated by the flow lines observed parallel to the lower and upper walls of the outlet zone (Figure 4) and the deviations of the flow lines observed in the elbows. The maximum value reached by the velocity u was 0.0085 m/s for both configurations in the y = 0.25 m position. For the velocity v, the maximum value reached was 0.014 m/s in the position y = 0.10 m.

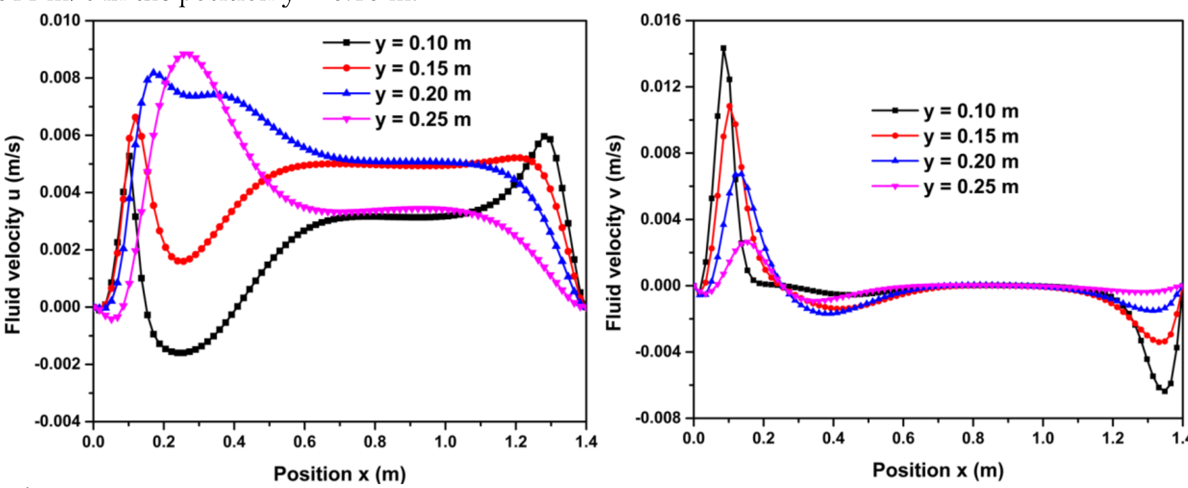

Figure 5.
Air velocity profiles at position x (mass flow 0.00967 kg/s, inlet fluid temperature 27°C and wind speed 1 m/s).

The variations in the u and v components of velocity as a function of the y-intercept are shown in Figure 6. Analysis of these figures shows that the profiles of u and v as a function of y are parabolic. The profiles of u have their peaks pointing upwards and the values of u as a function of y are positive. The values of velocity v as a function of y are negative. This velocity distribution explains the appearance of parallel streamlines near the upper wall dominated by forced convection. The maximum value reached by the velocity u was 0.009 m/s for both configurations in the position x = 0.009 m, while the maximum absolute value of the velocity v was 0.014 m/s in the position y = 0.56 m.

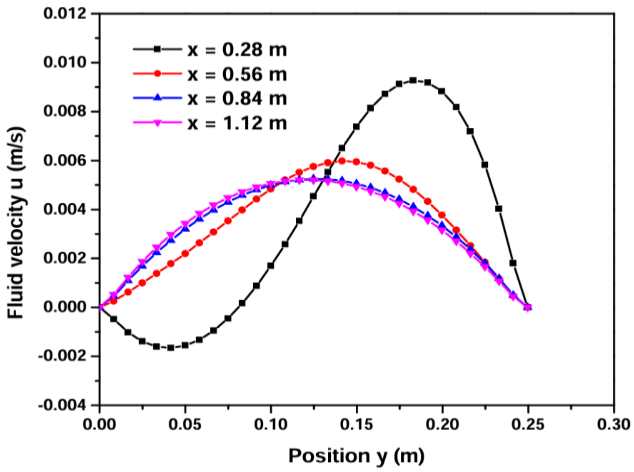

Figure 6.
Air velocity profiles at y position (mass flow 0.00967 kg/s, inlet fluid temperature 27°C and wind speed 1 m/s).

4.3. Temperature Analysis

Figure 7 shows the temperature variation as a function of time of the PV solar cells, the top cover (Glass) and bottom cover (Tedlar or Glass), the absorber plate, the outlet air, the confined air layer and the glass cover for the two configurations considered. The highest temperatures were obtained when the intensity of solar radiation was very high. The temperatures of all the layers of the Glass-PV-Tedlar flat-plate hybrid air collector are higher than those of the Glass-PV-Glass flat-plate hybrid air collector. This is due to the greater conductive heat transfer between the PV cells and the Tedlar than between the PV cells and the glass. The PV cells had a higher temperature than all other layers in both configurations which were respectively 55.25°C for the PVT Glass-PV-Glass hybrid collector (Figure 7 (b)) and 62°C for the PVT Glass-PV-Tedlar hybrid collector (Figure 7 (a)) around 12:00. These results clearly show that the PVT Glass-PV-Glass hybrid collector cools the PV solar cells much more than the PVT Glass-PV-Tedlar hybrid collector.

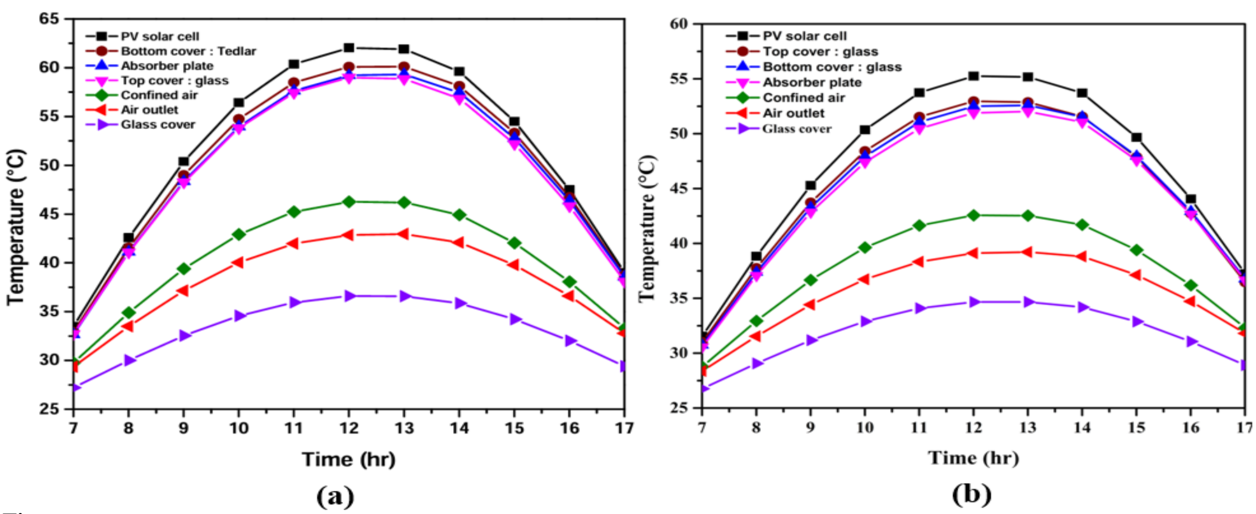

Figure 7.
Variations in layer temperatures at different positions as a function of time for the two PVT hybrid collector configurations: (a) Glass-PV-Tedlar (b) Glass-PV-Glass (mass flow rate 0.00967 kg/s, inlet fluid temperature 27 °C and wind speed 1 m/s).

Figure 8 shows the isotherms of the heat transfer fluid in the channel. The analysis of this figure indicates the presence of isothermal lines parallel to the lower and upper walls of the PVT hybrid collector cavity that are slightly deformed in the curves of the cavity. This distribution reveals that the heat transfers are mainly by convection in the heat transfer fluid. It is also noted that isotherms are normal to the left and right walls of the different areas of the sensor cavity since these walls are adiabatic. Isotherm values increase from the metal bottom wall to the glass top wall. This result is explained by the fact that the solar flux is imposed on the upper part of the sensor. The heat is transmitted from close to close through the different elements of the sensor. This heat is then transmitted to the heat transfer air by convection and conduction explaining the rise in temperature of the fluid in the area close to the protective glass constituting the upper wall of the airflow channel.

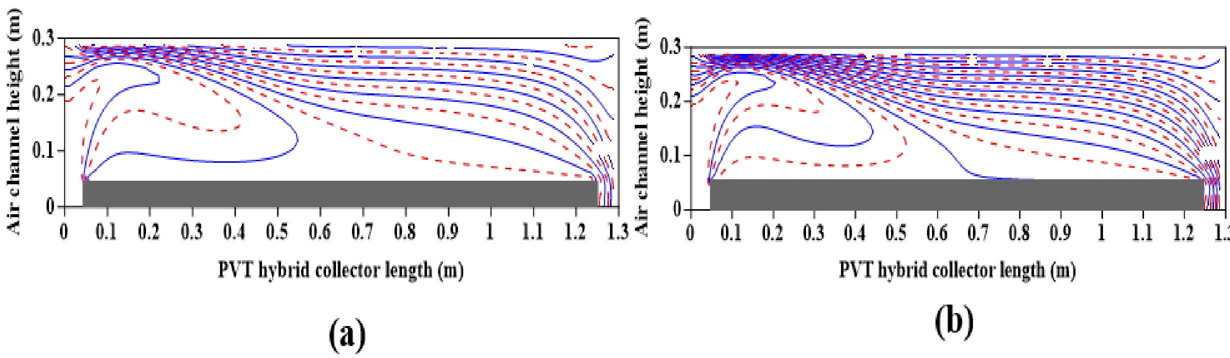

Figure 8.
Fluid isotherm distribution: (a) Glass-PV-Tedlar (b) Glass-PV-Glass (mass flow rate 0.00967 kg/s, inlet fluid temperature 27°C and wind speed 1 m/s).

Figure 9 shows the isotherms in the PV cell layer in both configurations studied. In both cases, temperature stratification is observed in this layer. The lowest temperatures are in the area near the heat exchanger. The temperature is 59.30°C for Glass-Tedlar-glass and 52.88°C for Glass-PV-Glass. In the upper area of the PV cells, temperatures are much higher. The temperature in this part of the PV cells is lower for Glass-PV-Glass (53.62 °C) than for Glass-PV-Tedlar (60.21 °C). This result is explained by the forced air convection cooling of PV cells and the low thermal conductivity of Tedlar compared to glass.

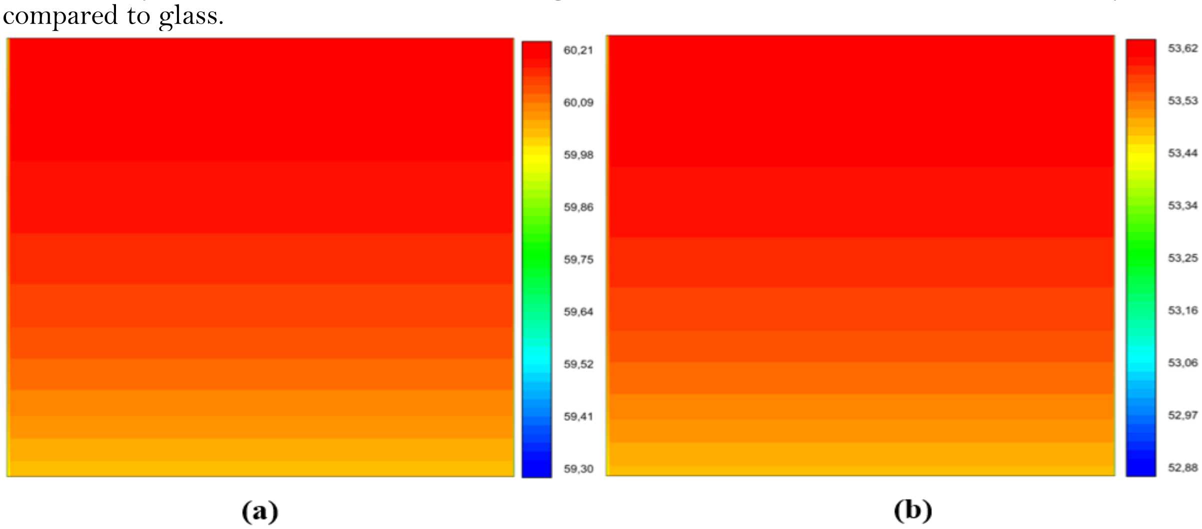

Figure 9.
PV solar cell temperature distribution at different positions of the two hybrid PVT collector configurations at 12:00: (a) Glass-PV-Tedlar (b) Glass-PV-Glass (mass flow rate of 0.00967 kg/s, inlet fluid temperature 27 °C and wind speed 1 m/s).

4.4. Effect of Replacing the Tedlar with A Glass

Figure 10 shows the daily variations in PV solar cell temperature and electrical efficiency for both the Glass-PV-Tedlar and Glass-PV-Glass configurations. We note that the temperature of PV solar cells increases to maximum values equal to 60°C and 53°C for both configurations, respectively, during periods of strong sunshine. It then begins to decrease as the sun's radiation decreases during the day. The temperature of PV solar cells negatively affects the electrical efficiency, that is, the electrical efficiency decreases when the temperature of PV solar cells increases. In addition, the PV solar cells of the hybrid PVT flat-air Glass-PV-Tedlar solar collector are very hot, which results in the low electrical efficiency of this configuration. Using glass instead of Tedlar improves its electrical efficiency (with an average deviation of 1.49 %). We can also note that the temperature of PV solar cells and electrical efficiency are close in both configurations, at the beginning and after 17:00, due to low sunshine.

Figure 11 shows the evolution of the outlet temperature used to cool PV solar cells, in both cases, during the day. It is clear that the temperature of the outlet air increases with increasing intensity of solar radiation and reaches a maximum value of 46°C with a thermal efficiency of 60% for the case of the Glass-PV-Tedlar and 42°C with a thermal efficiency of 45% for the Glass-PV-Glass, under strong sunshine.

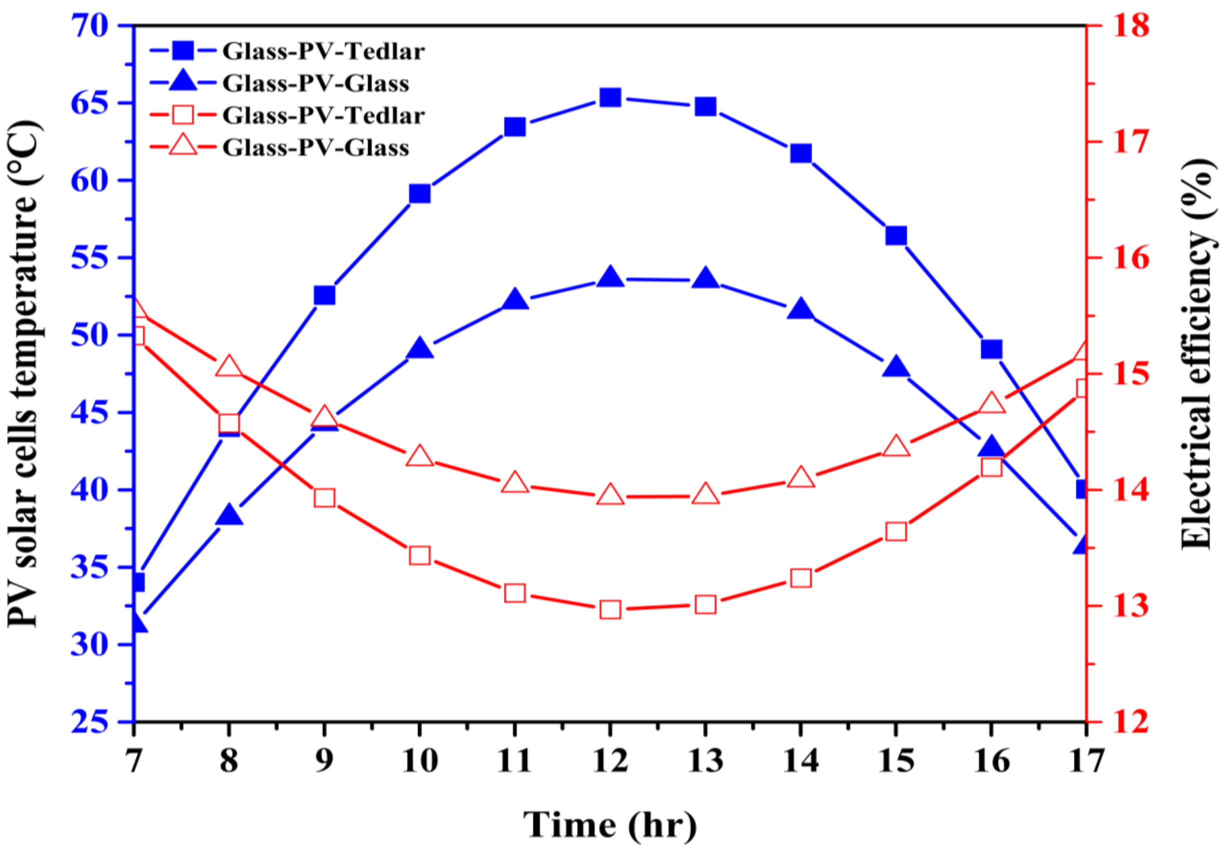

Figure 10.
Evolution of the temperature of PV solar cells and the electrical efficiency as a function of time in the two configurations of the hybrid PVT collector: (a) Glass-PV-Tedlar (b) Glass-PV-Glass (mass flow rate of 0.00967 kg/s, inlet fluid temperature 27 °C and wind speed 1 m/s).

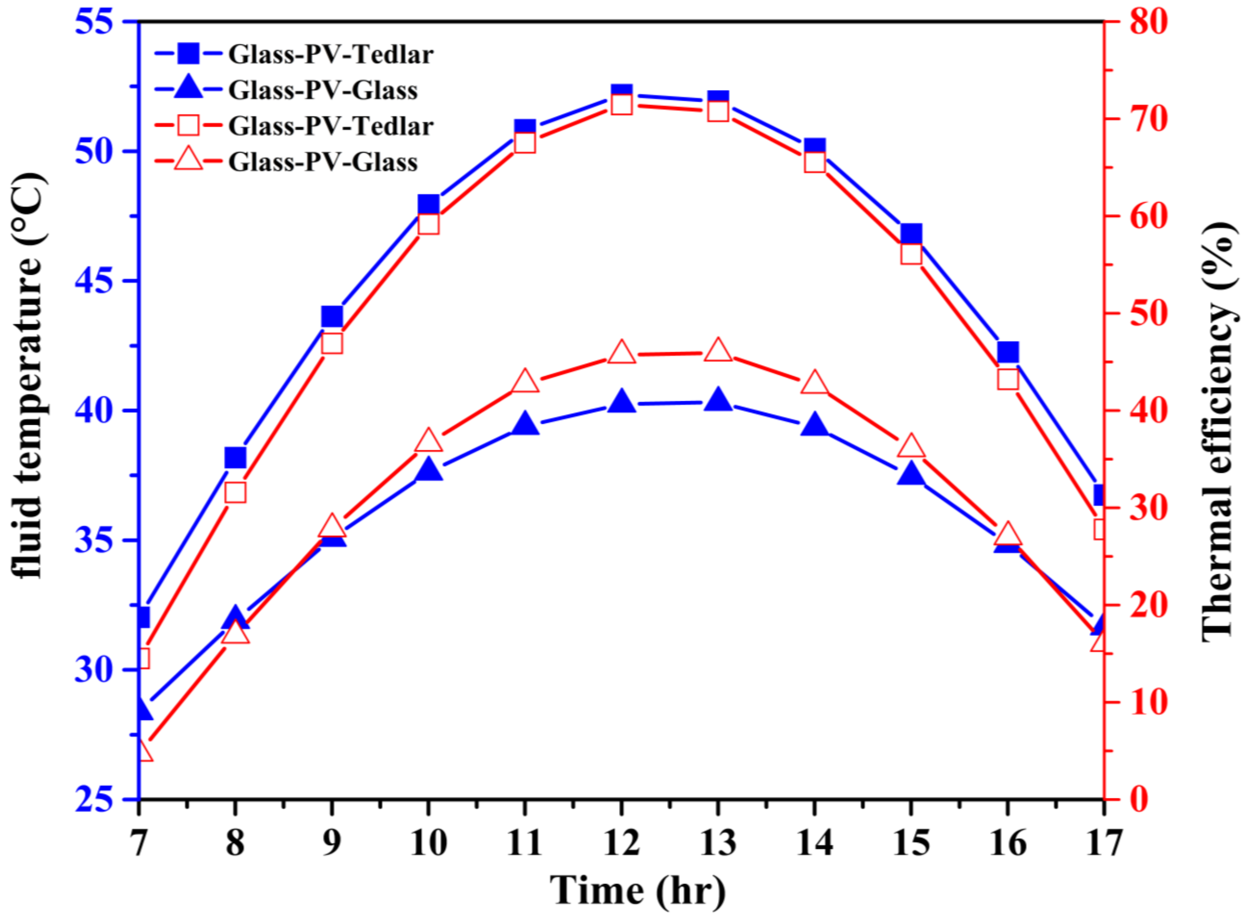

Figure 11.
Evolution of the fluid temperature at the outlet and the thermal efficiency as a function of time for the two configurations of the hybrid PVT collector: (a) Glass-PV-Tedlar (b) Glass-PV-Glass (mass flow rate of 0.00967 kg/s, inlet fluid temperature 27 °C and wind speed 1 m/s).

4.5. Energy Analysis

In the energy performance analysis of both configurations of the PVT flat-air hybrid collector, thermal power, electrical power, thermal efficiency and electrical efficiency are important parameters to evaluate.

Figure 12 shows the hourly variations in thermal power and electrical power for both configurations studied. Thermal power increased with the increase of incident solar radiation from 07:00 to 12:00, and decreased with the decrease of incident solar radiation from 12:00 to 17:00 in both configurations. The highest thermal powers were obtained at 12:00, which was the highest incident solar radiation of the day for both configurations. It was 100.88 W for the hybrid PVT Glass-PV-Glass collector and 130.80 W for the hybrid PVT Glass-PV-Tedlar collector. The highest power values were reached at 12:00 hours for both configurations. The electrical power obtained at 12:00 was 67.47 W for the hybrid Glass-PV-Glass PVT collector and 65.18 W for the hybrid Glass-PV-Tedlar PVT collector. The thermal power of the PVT Glass-PV-Tedlar hybrid collector was better than that of the PVT Glass-PV-Tedlar hybrid collector, while the electrical power of the PVT Glass-PV-Glass hybrid collector was much better than that of the PVT Glass-PV-Tedlar hybrid collector.

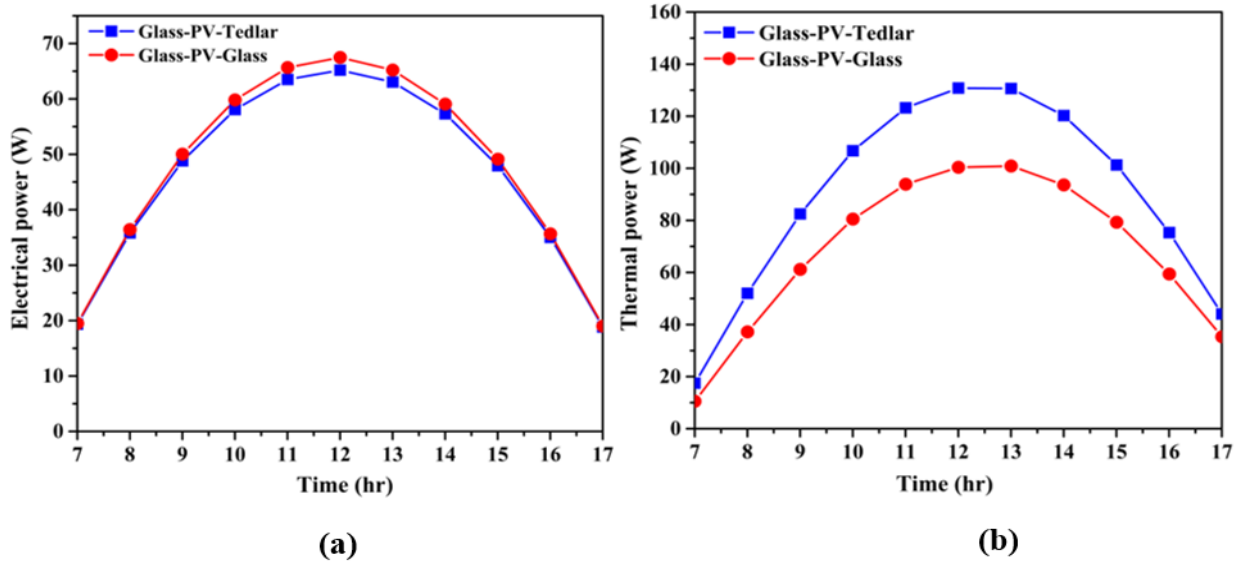

Figure 12.
Variations in thermal and electrical power as a function of time for both configurations: (a) thermal power and (b) electrical power (mass flow rate 0.00967 kg/s, fluid temperature at the inlet 27 °C and wind speed 1 m/s).

The hourly variations in electrical and thermal efficiency of both configurations are shown in Figure 13. The electrical yields of both configurations decreased from 07:00 to 12:00 and increased from 12:00 to 17:00. However, the electrical efficiency of the Glass-PV-Glass hybrid PVT collector (Figure 13 (a)) was significantly higher than that of the Glass-PV-Tedlar hybrid PVT collector. The lowest electrical efficiency for the Glass-PV-Glass hybrid PVT collector achieved was 15.34%, whereas for the Glass-PV-Tedlar hybrid PVT collector this value was reduced to 13.85% at 12:00. Due to the opaque nature of the tedlar, a large part of the incident solar radiation is intercepted, resulting in additional heat generation and thus a reduction in electrical efficiency. The highest daily thermal efficiency was 59.56% and 45.72% for the PVT Glass-PV-Tedlar hybrid collector and the PVT Glass-PV-Glass hybrid collector, respectively (Figure 13 (b)). The overall efficiency ranged from 23.38% to 73% for the Glass-PV-Tedlar hybrid PVT collector and 20.34% to 59.66% for the Glass-PV-Tedlar hybrid PVT collector (Figure 14 (a)). The maximum equivalent overall efficiency achieved by the Glass-PV-Tedlar Flat Air PVT Hybrid is 99% compared to 84.84% for the Glass-PV-Glass Flat Air PVT Hybrid (Figure 14 (b)).

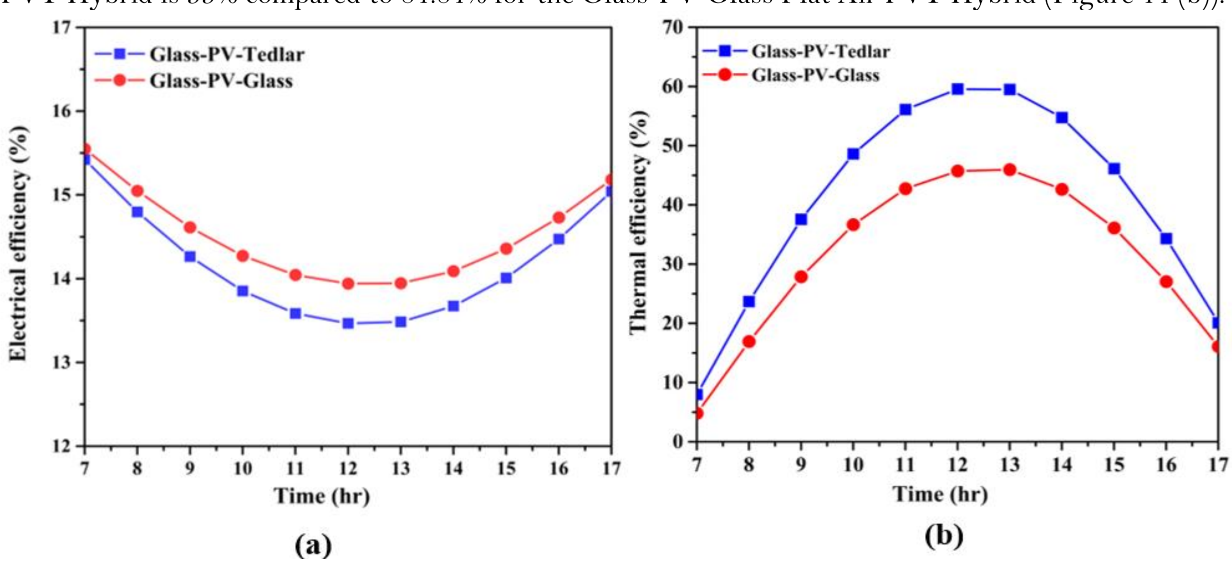

Figure 13.
Variations in (a) electrical and (b) thermal efficiency as a function of time (mass flow rate 0.00967 kg/s, inlet fluid temperature 27 °C and wind speed 1 m/s).

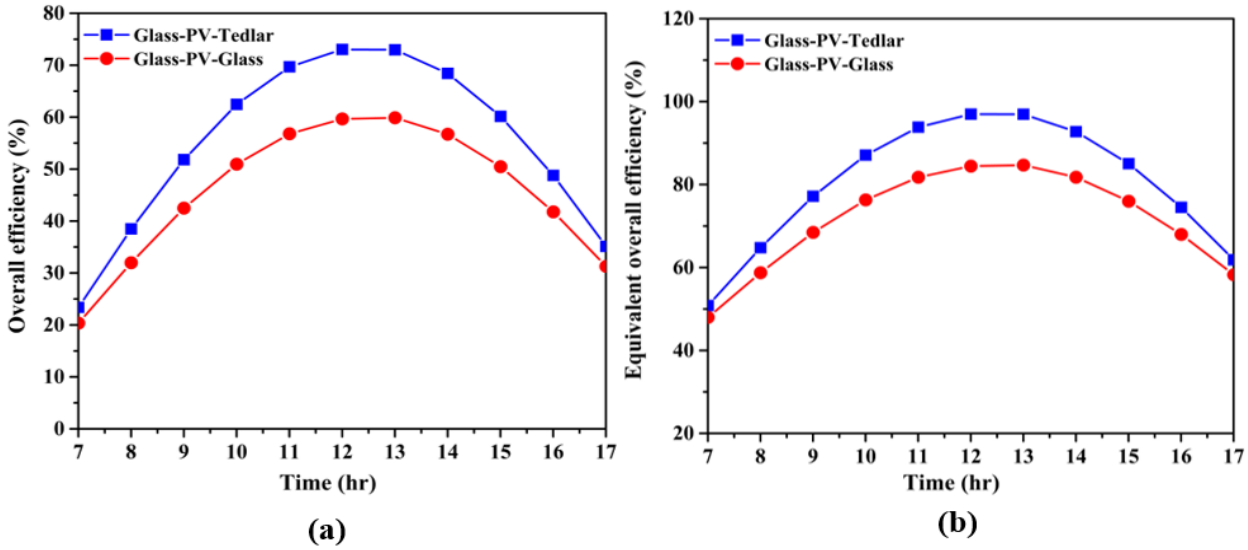

Figure 14.
Variations in (a) overall efficiency and (b) equivalent overall efficiency as a function of time (mass flow rate 0.00967 kg/s, fluid temperature at inlet 27 °C and wind speed 1 m/s).

4.6. Overall Energy Output

The daily average efficiencies are shown in Figure 15 (a) for both configurations. Note that the average thermal efficiency is higher than the average electrical efficiency. The overall efficiency share was 54.93% for the PVT Glass-PV-Tedlar hybrid collector and 45.65% for the PVT Glass-PV-Glass hybrid collector.

The daily useful energies in both configurations are shown in Figure 15 (b). The net heat gain depends on the ambient temperature; the higher the temperature difference between PV solar cells and the ambient air, the greater the thermal losses. The hybrid PVT flat-air Glass-PV-Tedlar collector had a useful energy gain of a daily average value of 0.548 kWh in electrical energy, 1.127 kWh in thermal energy and 1.675 kWh in overall energy, while the energy gain for the case of a hybrid PVT flat-air Glass-PV-Glass collector was 0.564 kWh in electrical energy, 0.839 kWh in thermal energy and 1.403 kWh in overall energy.

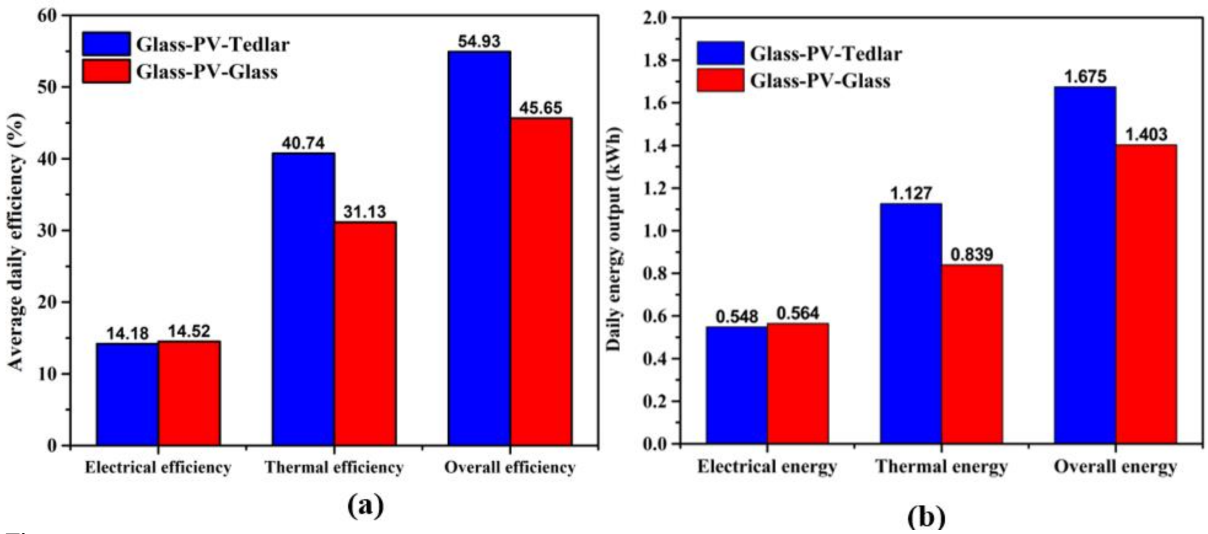

Figure 15.
(a) Daily average electrical, thermal and overall efficiencies of each configuration; (b) Daily production of thermal and electrical energy for each configuration (mass flow rate 0.00967 kg/s, fluid temperature at inlet 27 °C and wind speed 1 m/s).

5. Conclusion

This study compared two configurations of the PVT hybrid air flat-plat collector as part of the evaluation of their electrical and thermal performance. The integration of a two-glass protection in front and back of PV solar cells with an air heat exchanger minimizes the temperature of the photovoltaic cells and, consequently, increases the electrical performance of the PV solar module.

- The temperature of PV solar cells increases to maximum values equal to 60°C and 53°C for both the Glass-PV-Tedlar and Glass-PV-Glass configurations, respectively.
- Under the same operating conditions, the average electrical efficiency of the hybrid PVT glass-PV-glass and Glass-PV-Tedlar collector was 15.34% and 13.85%, respectively. There was a 1.49 % improvement in electrical efficiency for the Glass-PV-Glass hybrid PVT collector compared to the Glass-PV-Tedlar hybrid PVT collector.
- The hybrid PVT flat-air Glass-PV-Glass collector had a useful energy gain of a daily average value of 0.564 kWh in electrical energy and 0.839 kWh in thermal energy, while the energy gain for the case of the hybrid PVT flat-air Glass-PV-Glass was 0.548 kWh in electrical energy and 1.403 kWh in thermal energy.

The PVT hybrid collector-based cogeneration system is a complete energy system for supplying electrical and thermal energy to a home. The transient mathematical model presented is able to provide a real-time simulation of the hybrid flat-plate PVT air collector.

Funding:

The work was supported by funding from the World Bank for the project "Centre d'Excellence Régional pour la Maîtrise de l'Electricité (CERME)" of Universty of Lomé (Crédit IDA 6512-TG; Don IDA 536IDA).

Acknowledgment:

The authors gratefully acknowledge the support of all the staff of CERME and LES (Solar Energy Laboratory) for their assistance.

References

[1] International Energy Agency, AIE, "The global power mix will be transformed by 2028", *IEA*. 25 September 2024. https://www.iea.org/energy-system/renewables

[2] H. G. Teo, P. S. Lee and M. N. A. Hawlader, "An active cooling system for photovoltaic modules", *Applied Energy*, vol. 90, no 1, p. 309-315, 2012, doi: 10.1016/j.apenergy.2011.01.017.

[3] K. Hudon, "Solar Energy-Water Heating", *in Future Energy*, *Elsevier*, 2014, p. 433-451. doi: 10.1016/B978-0-08-099424-6.00020-X.

[4] E. Elsarrag, H. Pernau, J. Heuer, N. Roshan, Y. Alhorr and K. Bartholomé, "Spectrum splitting for efficient utilization of solar radiation: a novel photovoltaic-thermoelectric power generation system", *Renewables*, vol. 2, no 16, p. 1-11, 2015, doi: 10.1186/s40807-015-0016-y.

[5] D. Zenhäusern, E. Bamberger, A. Baggenstos and A. Häberle, "PVT Wrap-Up: Energy Systems with Photovoltaic Thermal Solar Collectors", *in Proceedings of SWC2017/SHC2017*, Abu Dhabi: International Solar Energy Society, 2017, p. 1-12. doi: 10.18086/swc.2017.18.12.

[6] S. A. Kalogirou, "Solar thermal collectors and applications", *Progress in Energy and Combustion Science*, vol. 30, no 3, p. 231-295, 2004, doi: 10.1016/j.pecs.2004.02.001.

[7] F. Shan, F. Tang, L. Cao and G. Fang, "Comparative simulation analyses on dynamic performances of photovoltaic-thermal solar collectors with different configurations", *Energy Conversion and Management*, vol. 87, p. 778-786, 2014, doi: 10.1016/j.enconman.2014.07.077.

[8] E. Dadioti, "Development of a pc-program for estimating the performance of water cooled Photovoltaic/Thermal systems", *M.Sc. in Renewable Energy and Architecture*, The University of Nottingham, Department of Architecture and Built Environment, 2010.

[9] S. Ranganathan, N. Elumalai and P. N. Priyadharshini, "Numerical model and experimental validation of the heat transfer in air cooled solar photovoltaic panel", *Therm sci*, vol. 20, no 4, p. 1071-1081, 2016, doi: 10.2298/TSCI16S4071R.

[10] A. Tiwari and M. S. Sodha, "Parametric study of various configurations of hybrid PV/thermal air collector: Experimental validation of theoretical model", *Solar Energy Materials and Solar Cells*, vol. 91, no 1, p. 17-28, 2007, doi: 10.1016/j.solmat.2006.06.061.

[11] A. S. Joshi, A. Tiwari, G. N. Tiwari, I. Dincer and B. V. Reddy, "Performance evaluation of a hybrid photovoltaic thermal (PV/T) (glass-to-glass) system", *International Journal of Thermal Sciences*, vol. 48, no 1, p. 154-164, 2009, doi: 10.1016/j.ijthermalsci.2008.05.001.

[12] J.-H. Kim and J.-T. Kim, "Comparison of Electrical and Thermal Performances of Glazed and Unglazed PVT Collectors", *International Journal of Photoenergy*, vol. 2012, p. 1-7, 2012, doi: 10.1155/2012/957847.

[13] M. E. A. Slimani, M. Amirat and S. Bahria, "Study and modeling of heat transfer and energy performance in a hybrid pv/t collector with double passage of air", *Inter J Ener Clean Env*, vol. 16, no 1-4, p. 235-245, 2015, doi: 10.1615/InterJEnerCleanEnv.2015015642.

[14] M. I. Hussain and J.-T. Kim, "Performance Evaluation of Photovoltaic/Thermal (PV/T) System Using Different Design Configurations", *Sustainability*, vol. 12, no 22, p. 9520, 2020, doi: 10.3390/su12229520.

[15] M. M. Hegazy, A. El-Sebaii, M. R. Ramadan, S. Aboul-Enein and A. E.-M. Khallaf, "Comparative study of three different designs of a hybrid PV/T double-pass finned plate solar air heater", *Environ Sci Pollut Res*, vol. 27, no 26, p. 32270-32282, 2020, doi: 10.1007/s11356-019-07487-8.

[16] R. Beniwal, G. N. Tiwari and H. O. Gupta, "Overall efficiency enhancement and cost optimization of semitransparent photovoltaic thermal air collector", *ETRI Journal*, vol. 42, no 1, p. 118-128, févr. 2020, doi: 10.4218/etrij.2018-0540.

[17] M. A. El-Hamid, G. Wei, M. Sherin, L. Cui and X. Du, "Comparative study of different photovoltaic/thermal hybrid configurations from energetic and exergetic Points of view: A Numerical Analysis", *Journal of Solar Energy Engineering*, vol. 143, no 6, p. 1-12, 2021, doi: 10.1115/1.4051154.

[18] R. Hossain, E. Ahmed, S.M.S. Islam, N. Saha, P. Debnath, A. Kouzani, M.P. Mahmud, "New Design of Solar Photovoltaic and Thermal Hybrid System for Performance Improvement of Solar Photovoltaic", International Journal of Photoenergy, 2020, doi: 10.1155/2020/8825489.

[19] A. Nahar, M. Hasanuzzaman and N. A. Rahim, "A Three-Dimensional Comprehensive Numerical Investigation of Different Operating Parameters on the Performance of a Photovoltaic Thermal System With Pancake Collector", *Journal of Solar Energy Engineering*, vol. 139, no 3, p. 1-15, 2017, doi: 10.1115/1.4035818.

[20] A. Nahar, "Numerical investigation and modelling of solar photovoltaic/thermal systems", Doctor of philosophy, Institute of Graduate Studies, University of Malaya, Kuala Lumpur, Kuala Lumpur, 2017.

[21] S. R. Maadi, M. Khatibi, E. Ebrahimnia-Bajestan and D. Wood, "Coupled thermal-optical numerical modeling of PV/T Module-Combining CFD approach and two-band radiation DO model", *Energy Conversion and Management*, vol. 198, p. 111781, oct. 2019, doi: 10.1016/j.enconman.2019.111781.

[22] N. Boulfaf, J. Chaoufi, A. Ghafiri and A. Elorf, "Thermal Study of Hybrid Photovoltaic Thermal (PV-T) Solar Air Collector Using Finite Element Method", *IJRER*, vol. 6, no 1, 2016, doi: 10.20508/ijrer.v6i1.3294.g6793.

[23] J. Dobrianski, "Simulation of the influence of design and meteorological factors on the efficiency of a solar plate collector", *Archives of Thermodynamics*, vol. 30, no 2, p. 1-30, 2009.

[24] H. B. C. El Hocine and M. Marir-Benabbas, "Study of Various Configurations of Hybrid PV/T System", *International Journal of Materials*, vol. 8, p. 62-69, 2021, doi: 10.46300/91018.2021.8.8.
[25] A. Nahar, M. Hasanuzzaman, N. A. Rahim and S. Parvin, "Numerical investigation on the effect of different parameters in enhancing heat transfer performance of photovoltaic thermal systems", *Renewable Energy*, vol. 132, p. 284-295, 2019, doi: 10.1016/j.renene.2018.08.008.
[26] M. Lyes, K. Tahar, H. Ouided and C. Hamid, "Effect of Air Channel Depth and Mass Flow Rate on the Efficiency of Hybrid Thermal - Photovoltaic Sensor", *IJM*, vol. 12, no 2, p. 147-168, 2018, doi: 10.21152/1750-9548.12.2.147.
[27] F. P. Incropera, David. Dewitt, T. L. Bergman and A. S. Lavine, "Fundamentals of heat and mass transfer", 6th ed. Hoboken, NJ: John Wiley & Sons, Inc., 2007.
[28] J. A. Duffie and W. A. Beckman, "Solar Engineering of Thermal Processes" *Fourth Edition. in Solar Energy Laboratory.* University of Wisconsin-Madison: John Wiley & Sons, Inc., Hoboken, New Jersey, 2013.
[29] K. G. T. Hollands, T. E. Unny, G. D. Raithby and L. Konicek, "Free Convective Heat Transfer Across Inclined Air Layers", *Journal of Heat Transfer*, vol. 98, no 2, p. 189-193, 1976, doi: 10.1115/1.3450517.
[30] C. El Fouas, N. C. Cherecheş, S. V. Hudişteanu, B. Hajji, E. F. Ţurcanu and M. L. Cherecheş, "Numerical and Parametric Analysis for Enhancing Performances of Water Photovoltaic/Thermal System", *Applied Sciences*, vol. 12, no 2, 2022, doi: 10.3390/app12020646.
[31] K. S. Ong, "Thermal Performance of Solar air Heaters: Mathematical Model and Solution Procedure", vol. 55, no 2, p. 93-109, 1995, doi: https://doi.org/10.1016/0038-092X(95)00021-I.
[32] S. Kalogirou, "Solar energy engineering: processes and systems", *Second edition. Amsterdam; Boston: Elsevier*, AP, Academic Press is an imprint of Elsevier, 2014.
[33] E. Skoplaki and J. A. Palyvos, "On the temperature dependence of photovoltaic module electrical performance: A review of efficiency/power correlations", *Solar Energy*, vol. 83, no 5, p. 614-624, 2009, doi: 10.1016/j.solener.2008.10.008.
[34] T. T. Chow, "A review on photovoltaic/thermal hybrid solar technology", *Applied Energy*, vol. 87, no 2, p. 365-379, 2010, doi: 10.1016/j.apenergy.2009.06.037.
[35] M. Al-Damook, D. Dixon-Hardy, P.J. Heggs, M. Al Qubeissi, K. Al-Ghaithi, P.E. Mason, J. Cottom, S. Grądziel, S. Łopata, T. Sobota, W. Zima, "CFD analysis of a one-pass photovoltaic/thermal air system with and without offset strip fins", *MATEC Web of Conferences*, vol. 240, p. 1-5, 2018, doi: 10.1051/matecconf/201824003002.
[36] A. Fudholi, M.F. Musthafa, G.L. Jin, R. Darussalam, A. Rajani, Anwar, M.H. Yazdi, H. Moria, M.Y. Othman, M.H. Ruslan, K. Sopian, "Experimental and model validation of photovoltaic-thermal (PVT) air collector: exergy analysis", *J. Mechatron. Electr. Power Veh. Technol.*, vol. 12, no 1, p. 10-17, juill. 2021, doi: 10.14203/j.mev.2021.v12.10-17.